FLOWFIELD OF A LIFTING HOVERING ROTOR— A NAVIER-STOKES SIMULATION

G. R. Srinivasan,* J. D. Baeder,** S. Obayashi,† and W. J. McCroskey**
NASA Ames Research Center, Moffett Field, California 94035, U.S.A.

Abstract

The viscous, three-dimensional flow field of a lifting helicopter rotor in hover is calculated by using an upwind, implicit, finite-difference numerical method for solving the thin layer Navier-Stokes equations. The induced effects of the wake, including the interaction of tip vortices with successive blades, are calculated as a part of the overall flowfield solution without using any ad hoc wake models. Comparison of the numerical results for the subsonic and transonic conditions show good agreement with the experimental data and with the previously published Navier-Stokes calculations using a simple wake model. Some comparisons with Euler calculations are also presented, along with some discussions of the grid refinement studies.

Introduction

The accurate numerical simulation of the flowfield of a lifting helicopter rotor continues to be one of the most complex and challenging problems of applied aerodynamics. This is true in spite of the availability of the present day supercomputers of Cray-2 class and improved numerical algorithms. However, many advances have been made to date with the use of simpler set of equations of fluid motion, such as the potential flow equations, to model these complex flowfields. The equations have been simplified by coupling the solution scheme with an empirical wake model to bring in the influence of the vortex wake. Solution schemes that use this idea are often grouped under methods using wake models and encompass the potential flow (Refs. 1-5), the Euler (Refs. 6-8) and the Navier-Stokes methods (Refs. 9-12). In contrast to these methods that use ad hoc wake models, there are methods that compute the essential details of the induced effects of vortex wake as a part of the overall flowfield solution. These are called the wake capturing schemes and have been demonstrated for the solutions of the potential flow (Ref. 13), the Euler (Refs. 14-17) and the Navier-Stokes equations (Ref. 18).

The basic assumptions of potential flow methods restrict their application to low supercritical speeds without the use of entropy corrections. Despite this feature, the potential flow methods, coupled with a wake modeling, have been very useful in the industrial environment for design analysis (Refs. 2-5). On the other hand, the Euler equations contain the essential physics to describe convection of vortical flows and do not have the restriction on the Mach number. But they still lack the essential ingredients to model the separated flows and inviscid-viscous interactions associated with shock-induced separated flows. Nevertheless, the Euler methods have been used to model these complex vortical flows by coupling with wake models (Refs. 6-8) as in potential flow methods. But the major drawback of these methods is that they have proven to be more expensive in comparison to the potential flow methods.

Even Navier-Stokes methods (Refs. 9-12) have been coupled with wake models to calculate these complex flows. Although these methods capture viscous effects adequately, they remain limited by the wake modeling, which tends to be restricted to simple geometries and planforms. In general, a major disadvantage of these methods which use wake modeling is that the technique of prescribing a wake has to be specialized for each blade shape and planform and therefore cannot easily handle arbitrary blade shapes with twist or taper.

Therefore, the weak link in the above wake-coupled methodologies has been the wake modeling. In contrast to the methods using wake modeling, several schemes have attempted to capture the wake and its effect as a part of the overall solution scheme. These methods range in complexity from potential flow methods (Ref. 13) to a Navier-Stokes method (Ref. 18). All of these inviscid methods (Refs. 13-17) utilize finite-volume formulation for the solution method. Of these different wake capturing schemes, the potential flow scheme of Ramachandran et al. (Ref. 13) appears to be the most accurate. All of the Euler methods appear to compute the flow in the tip region reasonably well. However, the inviscid methods still lack the ability to capture accurately the formation of a tightly-braided tip vortex structure, and therefore, the accuracy of the computed wake and tip-vortex core may be questionable.

The purpose of this study is to develop a calculation method for the solution of Navier-Stokes equations for the complete flowfield of a lifting rotor, including the wake and its induced effects. The vortex wake and its effects are captured as a part

*JAI Associates, Inc.
**U.S. Army Aeroflightdynamics Directorate.
†MCAT Institute.

of the complete flowfield, and thus no arbitrary inputs are necessary to describe the wake. Although this is not very different in concept from the Euler wake-capture schemes discussed above, the Navier-Stokes approach was needed for the following reasons: 1) better tip-flow simulation, which involves resolving the blade-tip separation and the formation of a concentrated tip vortex, 2) accurate simulation of strong viscous-inviscid interaction involving shock induced separation at high blade tip speeds and high collective pitch conditions, and 3) future modeling of retreating blade and dynamic stall regimes in forward flight.

The numerical code used in this study is an improvement of the version that was developed previously in related studies with wake modeling (Ref. 9). One fundamental difference of the new numerical scheme is the use of Roe's upwinding in all three directions (Ref. 19). This feature, coupled with a simplified left-hand-side, has produced an efficient and accurate numerical scheme. These additional changes in the Navier-Stokes algorithm are based on some of the numerical procedures described in Ref. 20 and will be described briefly in the following sections.

Governing Equations

The governing differential equations are the thin layer Navier-Stokes equations. These can be written in conservation-law form in a generalized body-conforming curvilinear coordinate system as follows (Ref. 21):

$$\partial_\tau \widehat{Q} + \partial_\xi \widehat{E} + \partial_\eta \widehat{F} + \partial_\zeta \widehat{G} = \frac{\epsilon}{Re}\partial_\zeta \widehat{S} \qquad (1)$$

where $\tau = t$, $\xi = \xi(x,y,z,t)$, $\eta = \eta(x,y,z,t)$ and $\zeta = \zeta(x,y,z,t)$. The coordinate system (x,y,z,t) is attached to the blade (see Fig. 1). The vector of conserved quantities $\widehat{Q}$ and the inviscid flux vectors $\widehat{E}$, $\widehat{F}$, and $\widehat{S}$ are given by

$$\widehat{Q} = \frac{1}{J}\begin{bmatrix} \rho \\ \rho u \\ \rho v \\ \rho w \\ e \end{bmatrix}, \qquad \widehat{E} = \frac{1}{J}\begin{bmatrix} \rho U \\ \rho u U + \xi_x p \\ \rho v U + \xi_y p \\ \rho w U + \xi_z p \\ U H - \xi_t p \end{bmatrix}$$

$$\widehat{F} = \frac{1}{J}\begin{bmatrix} \rho V \\ \rho u V + \eta_x p \\ \rho v V + \eta_y p \\ \rho w V + \eta_z p \\ V H - \eta_t p \end{bmatrix}, \widehat{G} = \frac{1}{J}\begin{bmatrix} \rho W \\ \rho u W + \zeta_x p \\ \rho v W + \zeta_y p \\ \rho w W + \zeta_z p \\ W H - \zeta_t p \end{bmatrix} \qquad (2)$$

where H = (e + p) and $\epsilon = 0$ or 1 for the Euler or the Navier-Stokes equations, respectively. In these equations, U, V, and W are the contravariant velocity components defined, for example, as $U = \xi_t + \xi_x u + \xi_y v + \xi_z w$. The Cartesian velocity components are represented by u, v, and w and the density, pressure, and the total energy per unit volume by ρ, p, and e, respectively. The characteristic length and velocity scales are the rotor blade chord and the ambient sound speed, and p and ρ are nondimensionalized by their respective ambient values. The quantities ξ_x, ξ_y, ξ_z, ξ_t, etc. are the coordinate transformation metrics and J is the Jacobian of the transformation. For the thin layer approximation used here, the viscous flux vector $\widehat{S}$ is given by

$$\widehat{S} = \frac{1}{J}\begin{bmatrix} 0 \\ \mu m_1 u_\zeta + \frac{\mu}{3} m_2 \zeta_x \\ \mu m_1 v_\zeta + \frac{\mu}{3} m_2 \zeta_y \\ \mu m_1 w_\zeta + \frac{\mu}{3} m_2 \zeta_z \\ \mu m_1 m_3 + \frac{\mu}{3} m_2 (\zeta_x u + \zeta_y v + \zeta_z w) \end{bmatrix} \qquad (3)$$

with

$$m_1 = \zeta_x^2 + \zeta_y^2 + \zeta_z^2$$

$$m_2 = \zeta_x u_\zeta + \zeta_y v_\zeta + \zeta_z w_\zeta$$

$$m_3 = \frac{1}{2}(u^2 + v^2 + w^2)_\zeta + \frac{1}{Pr\,(\gamma - 1)}(a^2)_\zeta$$

where Re is the Reynolds number, Pr is the Prandtl number, γ is the ratio of specific heats, and a is the speed of sound. The fluid pressure, p is related to the conservative flow variables, $\widehat{Q}$, through the nondimensional equation of state for a perfect gas,

$$p = (\gamma - 1)\{\, e - \frac{\rho}{2}(u^2 + v^2 + w^2)\,\} \qquad (4)$$

For turbulent viscous flows, the viscosity coefficient μ in $\widehat{S}$ is computed as the sum of $\mu_l + \mu_t$ where the laminar viscosity, μ_l, is estimated using Sutherland's law and the turbulent viscosity, μ_t, is evaluated using the Baldwin-Lomax algebraic eddy viscosity model (Ref. 22).

Numerical Algorithm

A finite-difference, upwind, numerical algorithm is developed for the helicopter rotor applications. The evaluation of the inviscid fluxes is based on an upwind-biased flux-difference splitting scheme for the right-hand side while an LU-SGS (Lower-Upper - Symmetric Gauss-Seidel) scheme, suggested by Jameson and Yoon (Refs. 23-24), is used for the implicit operator. The van Leer MUSCL (monotone upstream-centered scheme for the conservative laws) approach (Ref. 25) is used to evaluate the conservative variables to obtain the second- or third-order accuracy with flux limiters so as to be TVD (total variation diminishing). The upwind-biased scheme used on the right-hand side was originally suggested by Roe (Ref. 26) and later extended to three-dimensional flows by Vatsa et al. (Ref. 19). The chief advantage of using upwinding is that it eliminates the addition of explicit numerical dissipation and is known to produce less

dissipative solution (Ref. 19). This feature, coupled with a fine grid description in the tip region, increases the accuracy of the wake simulation. A similar algorithm was used in the finite-volume Euler scheme of Ref. 17 to investigate the exact same problem studied here.

The space-discretized form of the differential equation, Eq. (1), is

$$\partial_\tau \hat{Q} = -\frac{\hat{E}_{j+\frac{1}{2}} - \hat{E}_{j-\frac{1}{2}}}{\Delta\xi} - \frac{\hat{F}_{k+\frac{1}{2}} - \hat{F}_{k-\frac{1}{2}}}{\Delta\eta} - \frac{\hat{G}_{l+\frac{1}{2}} - \hat{G}_{l-\frac{1}{2}}}{\Delta\zeta} + \frac{1}{Re}\frac{\hat{S}_{l+\frac{1}{2}} - \hat{S}_{l-\frac{1}{2}}}{\Delta\zeta} \tag{5}$$

where j, k, and l correspond to the ξ, η, and ζ coordinate directions, respectively.

The application of Roe's upwinding (Ref. 19) to the numerical flux of the inviscid terms results in the locally one-dimensional form and can be written, e.g., in the ξ direction, as

$$\hat{E}(Q_L, Q_R, (\nabla\xi/J)_{j+\frac{1}{2}}) = \frac{1}{2}[\hat{E}(Q_R, (\nabla\xi/J)_{j+\frac{1}{2}}) + \hat{E}(Q_L, (\nabla\xi/J)_{j+\frac{1}{2}}) - |A(Q_L, Q_R, (\nabla\xi/J)_{j+\frac{1}{2}})|(Q_R - Q_L)] \tag{6}$$

where A is the Roe-averaged Jacobian matrix and Q_L and Q_R are the left and right state variables. The scheme degenerates to the first-order accuracy if $Q_L = Q_j$ and $Q_R = Q_{j+1}$. Higher-order schemes can be constructed from a one-parameter family of interpolations for the primitive variables, ρ, u, v, w, and p. For example,

$$p_l = \{1 + \frac{\psi_j}{4}[(1-\kappa)\nabla + (1+\kappa)\Delta]\}p_j$$

$$p_r = \{1 - \frac{\psi_{j+1}}{4}[(1+\kappa)\nabla + (1-\kappa)\Delta]\}p_{j+1}$$

where ∇ and Δ are backward and forward difference operators, and κ is a parameter that controls the construction of higher-order differencing schemes. For example, to construct the third-order scheme in the present method, $\kappa = \frac{1}{3}$, Koren's differentiable limiter (Ref. 27) is used. The limiter ψ is calculated as

$$\psi_j = \frac{3\nabla p_j \Delta p_j + \epsilon}{2(\Delta p_j - \nabla p_j)^2 + 3\nabla p_j \Delta p_j + \epsilon} \tag{7}$$

where a small constant, typically $\epsilon = 10^{-6}$, is added to prevent the division by zero. Similar formulae are used for the other primitive variables. The viscous flux terms are discretized using second-order central-differencing (Ref. 21).

The time marching integration procedure uses the LU-SGS method. The details of this scheme are described elsewhere (Ref. 20). The final form of this algorithm can be written for a first-order time accurate scheme as

$$LDU\Delta\hat{Q}^n = -\Delta t RHS^n \tag{8}$$

where

$$L = I - \Delta t\hat{A}^-|_{j,k,l} + \Delta t\nabla_\xi\hat{A}^+ - \Delta t\hat{B}^-|_{j,k,l} + \Delta t\nabla_\eta\hat{B}^+ - \Delta t\hat{C}^-|_{j,k,l} + \Delta t\nabla_\zeta\hat{C}^+$$

$$D = [I + \Delta t(\hat{A}^+ - \hat{A}^- + \hat{B}^+ - \hat{B}^- + \hat{C}^+ - \hat{C}^-)|_{j,k,l}]^{-1}$$

$$U = I + \Delta t\hat{A}^+|_{j,k,l} + \Delta t\Delta_\xi\hat{A}^- + \Delta t\hat{B}^+|_{j,k,l} + \Delta t\Delta_\eta\hat{B}^- + \Delta t\hat{C}^+|_{j,k,l} + \Delta t\Delta_\zeta\hat{C}^-$$

where Δt is the time step, RHS represents the discretized steady state terms, e. g., Eq. (5), and n refers to the current time-level. Also, $A^+ = \frac{1}{2}(A + \sigma_\xi)$, $A^- = \frac{1}{2}(A - \sigma_\xi)$, $\sigma_\xi = |U| + ar_\xi + \varepsilon$, $\varepsilon = 0.01$ typically, and $r_\xi = \sqrt{\xi_x^2 + \xi_y^2 + \xi_z^2}$. As a result of the simplified form of the Jacobian terms, e.g., A^+, the block diagonal matrix D reduces to a scalar diagonal matrix. Thus this method requires only two (one forward and one backward) sweeps with scalar inversions and leads to less factorization error. Lastly, additional source terms have been introduced to account for the rotation of the blades because of the blade-fixed coordinate system used here.

The present numerical scheme uses a finite-volume method for calculating the metrics. The chief advantage of such a formulation is that the metrics, including the time metrics, can be formed accurately (Ref. 28), and this approach captures the free-stream accurately (Ref. 17). To be compatible with the present finite-difference numerical scheme, the metrics are evaluated at the grid nodes instead of the cell centers of a standard finite-volume method (Ref. 20). Also, the time metrics are evaluated in the same manner as in a finite-difference scheme, which is less expensive computationally than rigorous evaluation of the time metrics. However, free-stream subtraction is then required to restore accuracy to the time-metric terms.

The flowfield of a hovering rotor is initially quiescent (Ref. 29) and the evolution of the flowfield is monitored as the blade is set in motion. To take advantage of

the quasi-steady nature of the hovering rotor flowfield, a locally-varying time step is used in the integration procedure to accelerate convergence, as suggested in Ref. 30.

Grids and Boundary Conditions

Body-conforming grids were generated for the rotor blades using an elliptic solver. Because of the cylindrical nature of the flow of a hovering rotor, a C-H cylindrical grid topology was chosen, as in Ref. 17. In contrast to the experimental model rotor that has a square tip, the present numerical scheme approximates this as a bevel tip because of the H-topology of the grid in that direction (see Ref. 31).

The standard viscous grids used here had 217 grid points in the wrap around (along the chord) direction with 144 points on the body, 71 points in the spanwise (radial) direction with 55 points on the blade surface, and 61 points in the normal direction. The grid was clustered near the leading and trailing edges and near the tip region to resolve the tip vortex. It was also clustered in the normal direction to resolve the viscous flow near the blade surface. There are about 15 points in the boundary layer with a spacing of the first grid point from the surface equal to 5×10^{-5} chord (that translates to a $y^+ = O(1)$). A coarse grid was constructed from this fine viscous grid by removing every other point in all three directions. The inboard plane near the axis of rotation was located at a radial station equal to one chord. The grid outer boundaries were set at 8 chords in all directions. The same grids were used for the Euler calculations.

Figure 1 shows the coarse grid that was used in the computations. Because of the symmetry of the hovering flow and the periodic boundary condition described below, the calculations could be performed for only one blade. Figure 1a shows the cylindrical nature of the grid in the plane of the rotor, and Fig. 1b shows an isometric view of the grid boundary for a single blade. For clarity, the figure shows only the blade and side boundaries. The bottom surface and other grid line are omitted. Also shown is the coordinate system, where x is in the chordwise direction, y is in the radial direction, and z is in the normal direction. The blade motion is counterclockwise.

All the boundary conditions are applied explicitly. The radial inboard and far-field boundaries, as well as the upper boundary of the cylindrical mesh, are updated by means of a characteristic-type boundary condition procedure, although the Roe's upwinding used in the numerical procedure would otherwise treat the boundaries in a 1-D characteristic sense anyway. At the wall a no-slip boundary condition is used for the viscous calculations. The Euler calculations use an extrapolation of the contravariant velocities at the surface. The density at the wall is determined by a zeroth-order extrapolation. The pressure along the body surface is calculated from the normal momentum relation (see, for example, Ref. 21). The total energy is then determined from the equation of state.

To capture the information in the wake region of the blade, a periodicity condition is used to swap the information, after interpolation, at the front and back boundaries of the cylindrical grid topology (see Fig. 1b). This is also done in an explicit manner. At the bottom boundary, the scene of the far-field wake, an approximate condition based on the normal velocity is used. For an outflow condition, all conserved flow quantities are extrapolated from the grid interior except for the energy, which is calculated by prescribing the free-stream pressure. For inflow at this boundary, the free-stream (ambient) conditions are specified.

Results and Discussion

The test cases considered in this study correspond to the experimental model hover test conditions of Caradonna and Tung (Ref. 29). The experimental model consists of a two-bladed rigid rotor with rectangular-planform blades with no twist or taper. The blades are made of NACA 0012 airfoil sections with an aspect ratio of 6. Three experimental conditions were chosen from among the data: 1) tip Mach number $M_{tip} = 0.44$, collective pitch $\theta = 8°$, and the Reynolds number based on the tip speed, $\mathrm{Re} = 1.92\times10^6$; 2) $M_{tip} = 0.877$, $\theta = 8°$ and $\mathrm{Re} = 3.93\times10^6$; and 3) $M_{tip} = 0.794$, $\theta = 12°$ and $\mathrm{Re} = 3.55\times10^6$.

Fine Grid Navier-Stokes Results

Surface pressures are shown in Figs. 2-4 for the three experimental conditions considered. These calculations were done on a fine grid consisting of nearly one million points. Figure 2 shows the surface pressures for the conditions of $M_{tip} = 0.44$, $\theta = 8°$, and $Re = 1.92\times10^6$. In this figure, the present calculations are compared with the experimental data of Ref. 29 and the results from a previous Navier-Stokes calculation that used a simple wake model (Ref. 9). The present calculations agree well with the experimental data for all radial stations. There are some improvements in the results at $y/R = 0.50$ and 0.96 over the previous results from Ref. 9. It should be pointed out that the calculations of Ref. 9 used a O-O grid topology with nearly 700,000 grid points having a grid clustering similar to the present grid.

Figure 3 shows a comparison of surface pressures for the condition of $M_{tip} = 0.877$, $\theta = 8°$ and $Re = 3.93\times10^6$. At this transonic flow condition, the present calculations show excellent agreement with the experimental data for all radial stations. In contrast to the calculations of Ref. 9, the present results show shock locations and shapes that are well captured. The inboard regions of the flow are also predicted

more accurately; this indicates that the present computed wake is superior to the approximate wake model of Ref. 9.

Figure 4 shows a comparison of surface pressures for the condition of $M_{tip} = 0.794$, $\theta = 12°$ and $Re = 3.55 \times 10^6$. Because of the high collective pitch, this case is more severe in terms of the shock strength and shock-induced boundary layer separation, even though the tip speed is slightly less than the previous case. The results show good agreement of the calculations with the experimental data, especially near the tip.

Figure 5 shows the extent of shock-induced boundary layer separation for the transonic cases discussed above. These are delineated as surface particle flow details and are created by releasing fluid particle tracers at one grid point above the surface and forcing them to stay in that plane. Such a view mimics the surface oil flow details measured in a laboratory experiment. Figure 5a shows the details of this flow for the case of $M_{tip} = 0.877$ and $\theta = 8°$. The separation and reattachment locations are apparent in this figure. It is seen that this flow condition produces a mild shock-induced separation in the outboard part of the blade. In contrast, the shock-induced separation and viscous-inviscid interaction are much stronger for the case of $M_{tip} = 0.794$ and $\theta = 12°$. The surface particle flow pattern for this more severe case is shown in Fig. 5b. As seen, the extent of the separation is much larger for this flow condition than for the case of Fig. 5a. It is interesting, however, to note that the separation patterns in the tip region are approximately the same for these cases.

A general comparison of the present results with the experimental data can be made by examining the bound circulation distribution. Figure 6 shows such a plot of dimensionless circulation, $\Gamma/\Omega R^2$, as function of r/R for $\theta = 8°$ case and tip speeds of 0.44 and 0.877, corresponding to the data presented in Figs. 2-3. Here r is the radial distance from the rotation axis, R is the radius of the rotor, Ω is the constant angular velocity of the rotor, and Γ is the circulation. The integrated local lift values are used from both the coarse and fine grid calculations to compute the dimensionless circulation shown in Fig. 6. Also shown are the integrated data from the experiments, which were reported to be essentially independent of tip speed. The calculations show a fair agreement with the experiments, except in the inboard part of the blade. This suggests that only the near-field effects of the tip vortex are captured as well as desired. There are two possible reasons for the poor agreement in the inboard part of the blade. First, the vortex wake becomes diffused in the far-field grid, so its induced effect is significantly diminished. Second, the inboard plane boundary condition may be inadequate. In contrast to the experimental observation, the present calculations show some dependency on the blade tip speed.

In the tip region the agreement is also not very good. This may be due to the bevel tip that is used in the computation compared to the square-tipped blade in the experiments. Overall, however, the surface pressure distributions appear to agree better with the experiments than the bound-circulation distribution. Relatively minor discrepancies in the pressure distributions near the leading edge, where the experimental transducer locations are relatively sparse, seem to translate into significant differences in the circulation distribution.

The chief advantage of the Navier-Stokes methods is to predict the separated flow in the tip region and the associated detailed structure of the tip vortex. The prediction of the overall shed-wake geometry is the most important step in the process of accurate modeling of the complete hover flowfield. The ability to keep this shed wake (including the vortex structure) intact from diffusing due to the numerical dissipation is a more complex issue. The ability to convect this shed wake without numerical dissipation determines if the inflow in the inboard parts of the blade is correct.

Figure 7 shows a near-field view of the tip vortex particle path trajectory for the experimental conditions of $M_{tip} = 0.794$ and $\theta = 12°$ corresponding to Fig. 4. These trajectories are generated by releasing particles of fluid in the vicinity of the tip of the blade on both surfaces and allowing them to move freely in time and space. It is apparent from this that the particles released right on the tip become braided and stay together in the vicinity of the core. As observed before (Ref. 31), the process of formation of the tip vortex involves braiding of fluid particles from both upper and lower surface of the blade. As the process of braiding of fluid particles from upper and lower surfaces continues, the tip vortex lifts up from the upper surface and rolls inboard in the downstream wake.

After identifying the fluid particles in the vicinity of the core in Fig. 7, fewer particles were released on the tip of the blade in the proximity of the quarter-chord region to trace out a trajectory of the tip vortex path. Figure 8 show two views of this trajectory. The computed tip vortex trajectory in space for a single blade is shown in Fig. 8a. Figure 8b shows a view of the tip vortex looking from the top which highlights the contraction of the wake. The contraction of the wake at 180° and 360° azimuthal positions is approximately 12.8% and 18.2% of the radius, respectively, in agreement with the experimental observation of 12.5% and 17% for this flow condition.

Fine Grid *vs.* Coarse Grid Results

The results presented in the preceeding sections were calculated on a fine grid of nearly one million points. The initial test calculations were made primarily on a coarse Navier-Stokes grid of 109×36×31 size. This grid was generated by removing every other point from the fine grid in all three

directions. The outer dimensions of the grid and the grid topology are thus the same as for the previous fine grid.

Figure 9 shows a comparison of surface pressure distributions for the fine and coarse grids for the experimental condition of $M_{tip} = 0.877$, $\theta = 8°$ and $Re = 3.93 \times 10^6$. It is surprising to see such good agreement of the coarse grid results overall with those of the fine grid and with the experiments. In the regions where the shocks are very strong, there are slight differences as expected. The results inboard of $y/R = 0.50$ show a bigger difference as seen from Fig. 6. These quasi-steady results for the coarse grid took about one hour of CPU (central processor unit) time on the Cray-2 supercomputer.

Euler *vs.* Navier-Stokes Results

As discussed earlier, there have been several attempts to capture rotor wakes using Euler methods (Refs. 14-17). The vortex formation in the tip region of a wing or a helicopter blade is a result of complex three-dimensional separated flow, and it is not clear how the Euler methods are able to mimic viscosity and separation to produce a vortex structure. Nevertheless, these Euler methods have been able to predict the pressure distributions and spanwise blade loading reasonably well for the outer part of the blade. Against this background, a limited comparison of surface pressures has been made for the Euler and Navier-Stokes methods calculated on the same fine grid of about one million points. It may be noted that the Euler version of the code did not exhibit any stability problems with this fine Navier-Stokes grid.

A typical comparison of the Euler results with the Navier-Stokes results is presented in Fig. 10 for the experimental test condition of $M_{tip} = 0.877$, $\theta = 8°$, and $Re = 3.93 \times 10^6$. Because it neglects viscous-inviscid interaction, the Euler method overpredicts the shock wave strength and position for $y/R \geq 0.80$. Otherwise, the Euler results are in good agreement with the Navier-Stokes results, which show mild shock-induced separation for this flow condition (see Fig. 5a). The overall agreement of surface pressures certainly does not reflect the details of the flow near the blade surface, especially the separation pattern and vortex wake details as predicted by the Navier-Stokes method. The details of the wake structure need to be investigated further.

Conclusions

The lifting hovering rotor flowfield is calculated by means of an implicit, completely upwind, finite-difference numerical procedure for the solution of thin layer Navier-Stokes equations using a cylindrical C-H grid topology and body fixed coordinates. The vortex wake and its induced effects are captured as a part of the overall numerical solution by the use of a periodicity condition, and the method therefore does not use any ad hoc wake models. The present numerical results are in good agreement with the experimental data, and they represent an improvement over the previously published Navier-Stokes results that used a simple wake model. Therefore, the method is promising. However, several important issues such as drag, power, and the detailed wake geometry remain to be examined in detail.

The good agreement of the surface pressures predicted by the Euler method with those of Navier-Stokes results seems to suggest that the details of surface flow including separation and tip vortex details are not important for predicting airloads. This needs further investigation. The robustness of the present methodology for Euler calculations is also demonstrated. Comparison of coarse and fine grid results indicate that the farfield wake effects are not as well captured with coarse grids. The numerical method is fairly efficient and runs at 145 MFLOPS on the Cray-2 supercomputer. The quasi-steady Navier-Stokes calculations presented here for coarse and fine grids took approximately 1 hour and 15 hours of CPU time, respectively, on this machine.

Acknowledgments

The first author (GRS) would like to acknowledge the support of this research by the U.S. Army Research Office under Contracts DAAL03-88-C-0006 and DAAL03-90-C-0013. Computational time was provided by the Applied Computational Fluids Branch of NASA Ames Research Center.

References

1. Caradonna, F. X., Desopper, A., and Tung, C., "Finite Difference Modeling of Rotor Flows Including Wake Effects," Paper No. 2.7, *Eighth European Rotorcraft Forum*, Aix-en Provence, France, Aug. 1982.

2. Strawn, R. C. and Caradonna, F. X., "Conservative Full-Potential Modle for Unsteady Transonic Rotor Flows," *AIAA Journal*, Vol. 25, No. 2, Feb. 1987, pp. 193-198.

3. Strawn, R. C. and Tung, C., "The Prediction of Transonic Loading on Advancing Helicopter Rotors," NASA Technical Memorandum 88238, April 1986.

4. Chang, I-C. and Tung, C., "Numerical Solution of the Full-Potential Equation for Rotor and Oblique Wings using a New Wake Model," AIAA Paper 85-0268, Jan. 1985.

5. Egolf, T. A. and Sparks, S. P., "A Full Potential Flow Analysis with Realistic Wake Influence for Helicopter Rotor Airload Prediction," NASA Contractor Report 4007, Jan. 1987.

6. Chang, I-C. and Tung. C., "Euler Solution of the Transonic Flow for a Helicopter Rotor," AIAA Paper 87-0523, Jan. 1987.

7. Agarwal, R. K. and Deese, J. E., "Euler Calculations for a Flowfield of a Helicopter Rotor in Hover," *Journal of Aircraft*, Vol. 24, No. 4, April 1987, pp. 231-238.

8. Sankar, N. L., Wake, B. E., and Lekoudis, S. G., "Solution of the Unsteady Euler Equations for Fixed and Rotor Wing Configurations," *Journal of Aircraft*, Vol. 23, No. 4, April 1986.

9. Srinivasan, G. R. and McCroskey, W. J., "Navier-Stokes Calculations of Hovering Rotor Flowfields," *Journal of Aircraft*, Vol. 25, No. 10, October 1988, pp. 865-874.

10. Wake, B. E. and Sankar, N. L., "Solutions of the Navier-Stokes Equations for the Flow About a Rotor Blade," *Journal of the American Helicopter Society*, Vol. 34, No. 2, April 1989, pp. 13-23.

11. Agarwal, R. K. and Deese, J. E., "Navier-Stokes Calculations of the Flowfield of a Helicopter Rotor in Hover," AIAA Paper 88-0106, 1988.

12. Narramore, J. C. and Vermeland, R., "Use of Navier-Stokes Code to Predict Flow Phenomena Near Stall as Measured on a 0.658-Scale V-22 Tiltrotor Blade," AIAA Paper 89-1814, June 1989.

13. Ramachandran, K., Tung. C., and Caradonna, F. X., "Rotor Hover Performance Prediction Using a Free-Wake, Computational Fluid Dynamics Method," *Journal of Aircraft*, Vol. 26, No. 12, Dec. 1989, pp. 1105-1110.

14. Kramer, E., Hertel, J., and Wagner, S., "Computation of Subsonic and Transonic Helicopter Rotor Flow Using Euler Equations," *Vertica*, Vol. 12, No. 3, 1988, pp. 279-291.

15. Kroll, N., "Computation of the Flow Fields of Propellers and Hovering Rotors Using Euler Equations," Paper No. 28, *Twelfth European Rotorcraft Forum*, Garmisch-Partenkirchen, Federal Republic of Germany, Sept. 1986.

16. Roberts, T. W. and Murman, E. M., "Solution Method for a Hovering Helicopter Rotor Using the Euler Equations," AIAA Paper 85-0436, Jan. 1985.

17. Chen, C.-L. and McCroskey, W. J., "Numerical Simulation of Helicopter Multi-Bladed Rotor Flow," AIAA Paper 88-0046, Jan. 1988.

18. Chen, C. S., Velkoff, H. R. and Tung, C., "Free-Wake Analysis of a Rotor in Hover," AIAA Paper 87-1245, June 1987.

19. Vatsa, V. N., Thomas, J. L. and Wedan, B. W., "Navier-Stokes Computations of Prolate Spheroids at Angle of Attack," AIAA Paper 87-2627, Aug. 1987.

20. Obayashi, S., "Numerical Simulation of Underexpanded Plumes Using Upwind Algorithms," AIAA Paper 88-4360-CP, Aug. 1988.

21. Pulliam, T. H. and Steger, J. L., "Implicit Finite-Difference Simulations of Three-Dimensional Compressible Flow," *AIAA Journal*, Vol. 18, No. 2, Feb. 1980, pp. 159-167.

22. Baldwin, B. S. and Lomax, H., "Thin Layer Approximation and Algebraic Model for Separated Turbulent Flow," AIAA Paper 78-0257, Jan. 1978.

23. Jameson, A. and Yoon, S., "Lower-Upper Implicit Schemes with Multiple Grids for the Euler Equations," *AIAA Journal*, Vol. 25, No. 7, July 1987, pp. 929-935.

24. Yoon, S. and Jameson, A., "An LU-SSOR Scheme for the Euler and Navier-Stokes Equations," AIAA Paper 87-0600, Jan. 1987.

25. Anderson, W. K., Thomas, J. L. and van Leer, B., "A Comparison of Finite Volume Flux Vector Splittings for the Euler Equations," AIAA Paper 85-0122, Jan. 1985.

26. Roe, P. L., "Approximate Riemann Solvers, Parameter Vectors, and Difference Schemes," *Journal of Computational Physics*, Vol. 43, 1981, pp. 357-372.

27. Koren, B., "Upwind Schemes, Multigrid and Defect Correction for the Steady Navier-Stokes Equations," *Proceedings of 11th International Conference on Numerical Methods in Fluid Dynamics*, June 1988.

28. Vinokur, M., "An Analysis of Finite-Difference and Finite-Volume Formulations of Conservation Laws," *Journal of Computational Physics*, Vol. 81, No. 1, Mar. 1989, pp. 1-52.

29. Caradonna, F. X. and Tung, C., "Experimental and Analytical Studies of a Model Helicopter Rotor in Hover," NASA Technical Memorandum 81232, Sept. 1981.

30. Srinivasan, G. R., Chyu, W. J. and Steger, J. L., "Computation of Simple Three-Dimensional Wing-Vortex Interaction in Transonic Flow," AIAA Paper 81-1206, June 1981.

31. Srinivasan, G. R., McCroskey, W. J., Baeder, J. D., and Edwards, T. A., "Numerical Simulation of Tip Vortices of Wings in Subsonic and Transonic Flows," *AIAA Journal*, Vol. 26, No. 10, Oct. 1988, pp. 1153-1162.

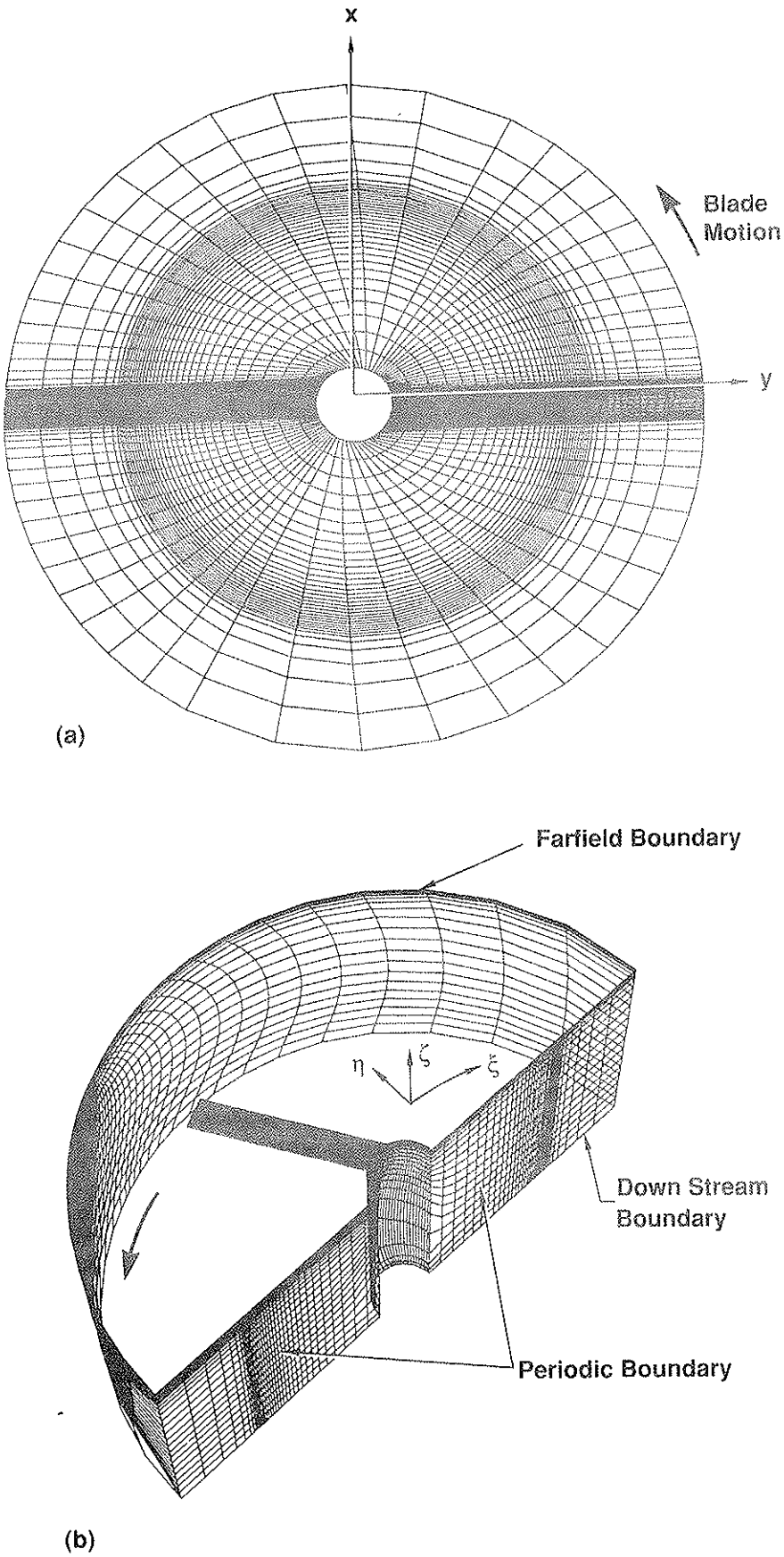

Fig. 1 Coarse C-H cylindrical grid topology for a two-bladed rotor; a) view in the plane of the rotor, and b) isometric view showing the grid boundaries for a single blade.

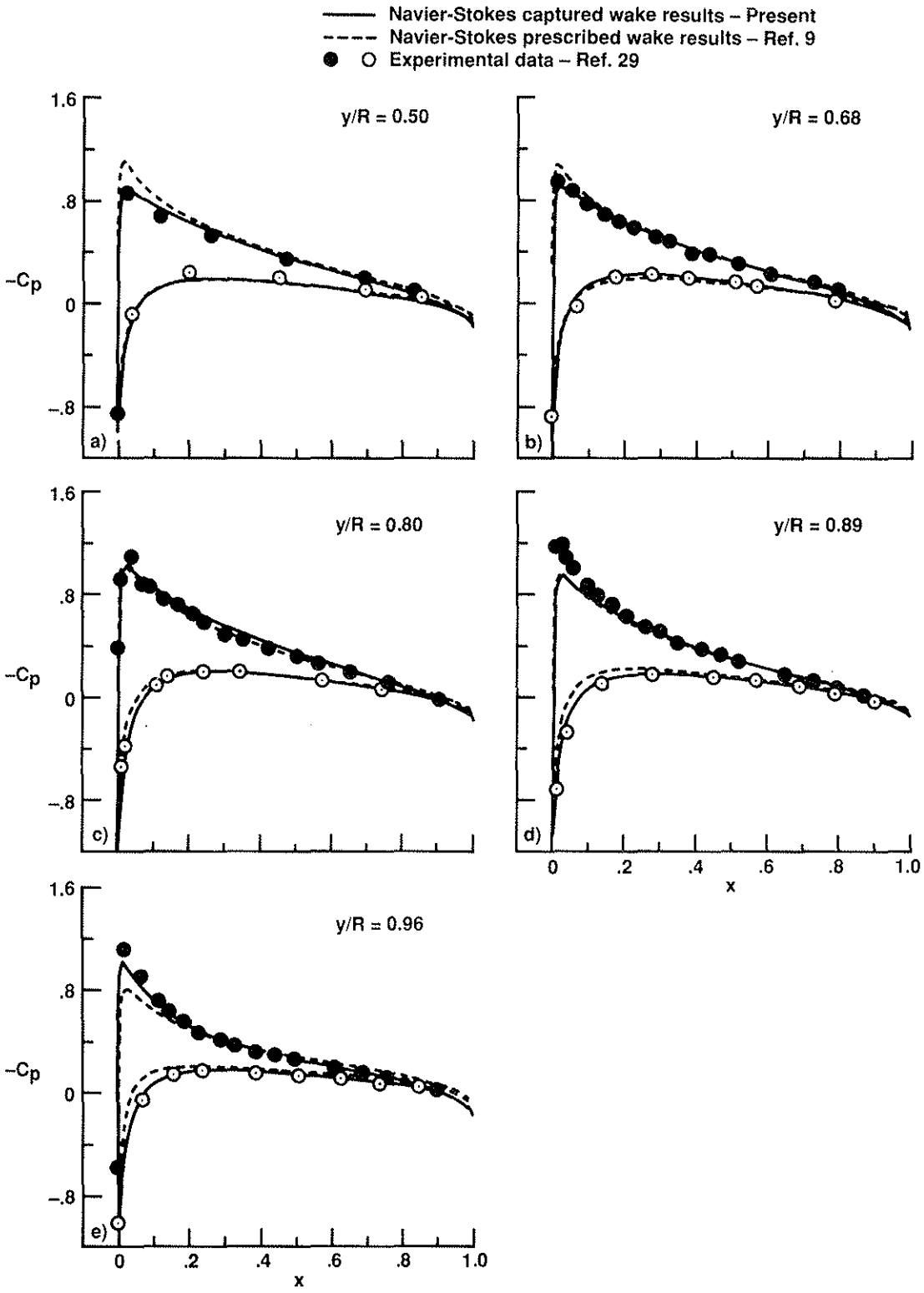

Fig. 2 Comparison of surface pressures for a lifting hovering rotor; $M_{tip} = 0.44$, $\theta = 8°$, and $Re = 1.92 \times 10^6$.

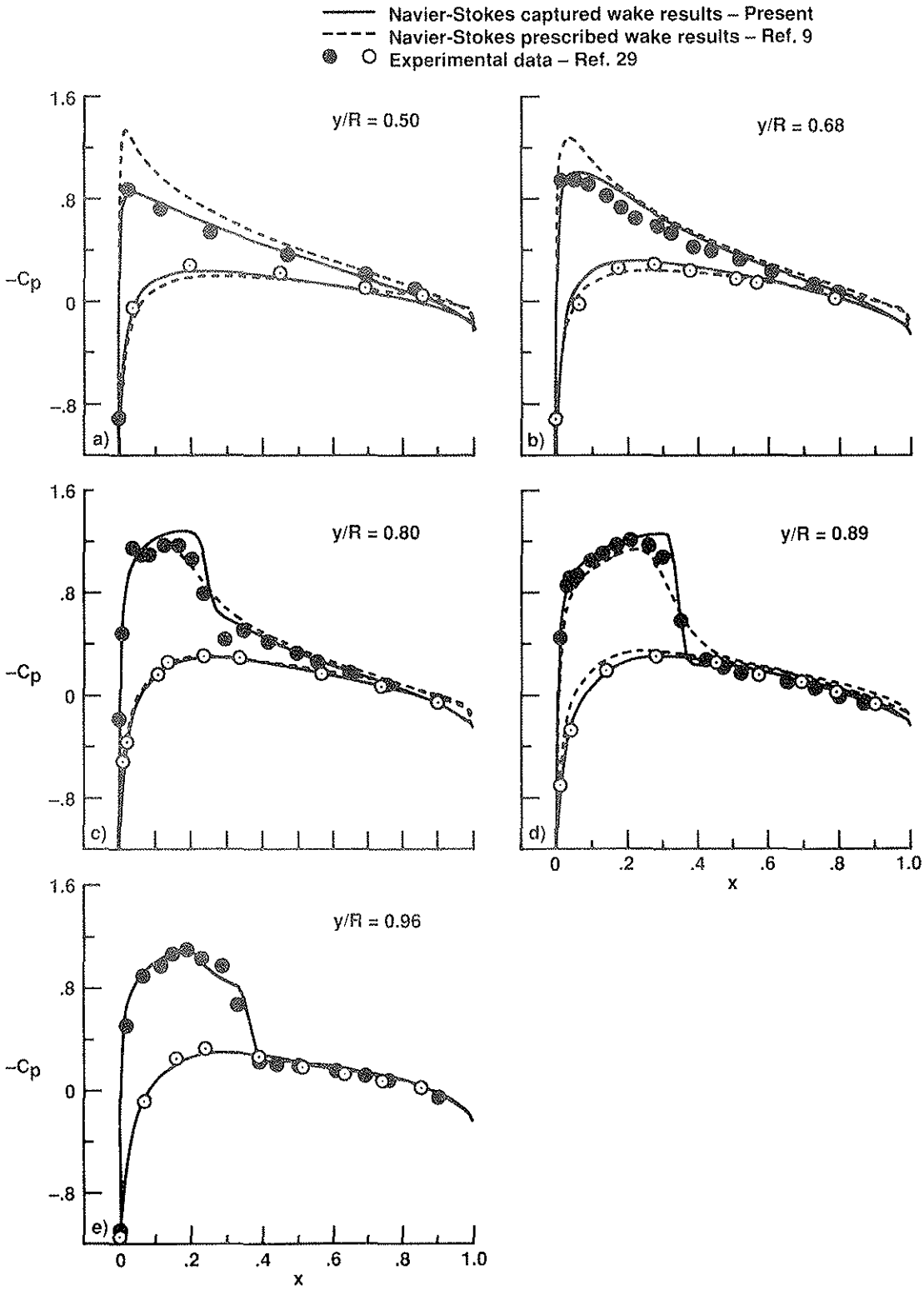

Fig. 3 Comparison of surface pressures for a lifting hovering rotor; $M_{tip} = 0.877$, $\theta = 8°$, and $Re = 3.93 \times 10^6$.

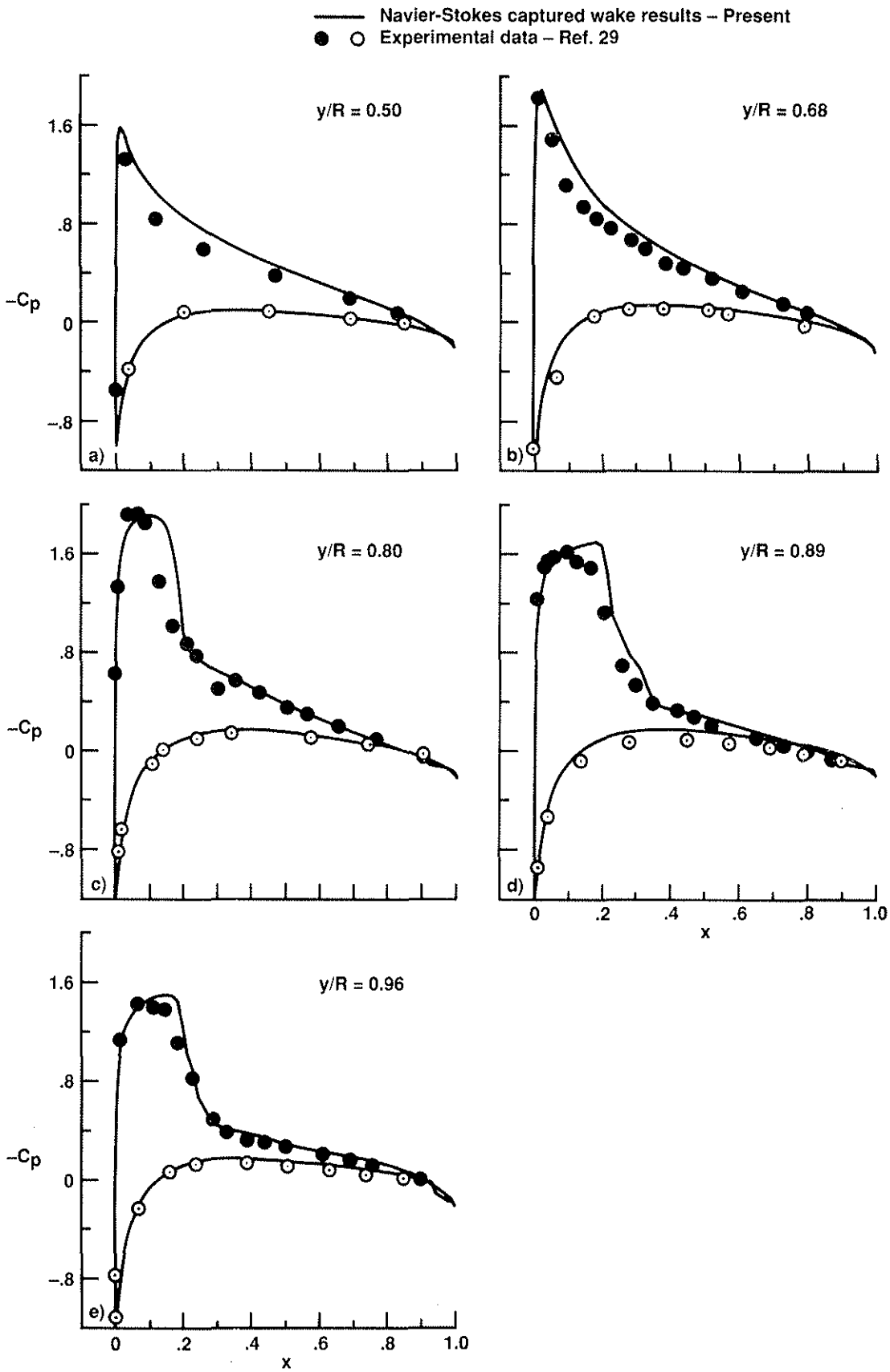

Fig. 4 Comparison of surface pressures for a lifting hovering rotor; $M_{tip} = 0.794$, $\theta = 12°$, and $Re = 3.55 \times 10^6$.

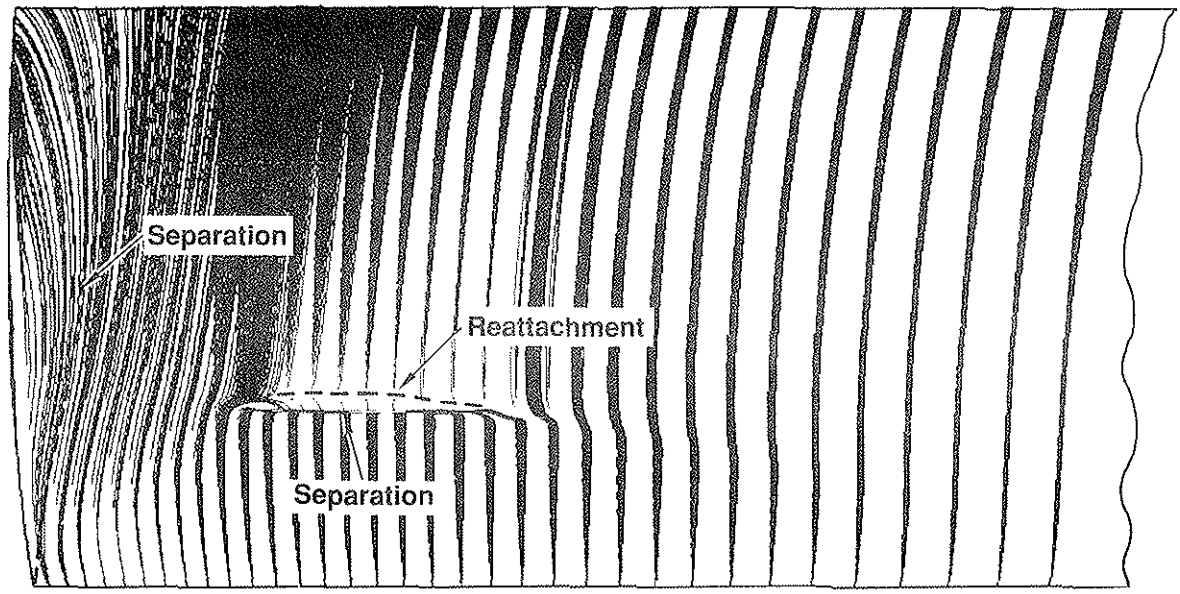

(a)

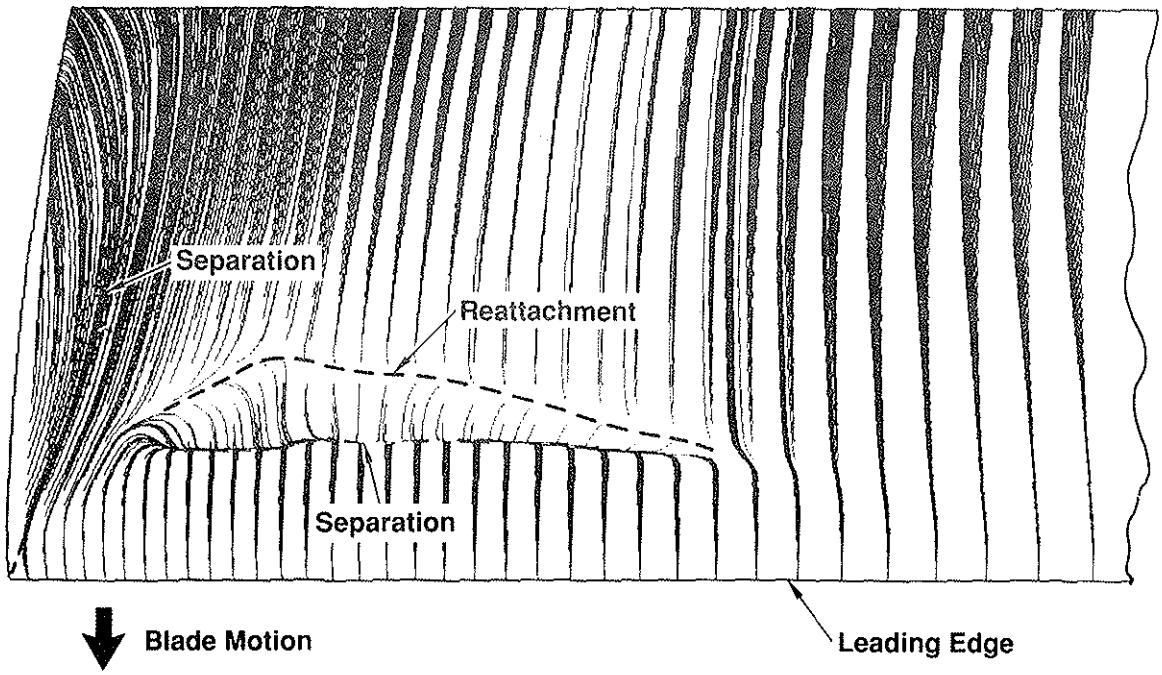

(b)

Fig. 5 Computed surface particle flow detail highlights the shock-induced boundary layer separation for the flow conditions of a) $M_{tip} = 0.877$, $\theta = 8°$, and $Re = 3.93 \times 10^6$, and b) $M_{tip} = 0.794$, $\theta = 12°$, and $Re = 3.55 \times 10^6$.

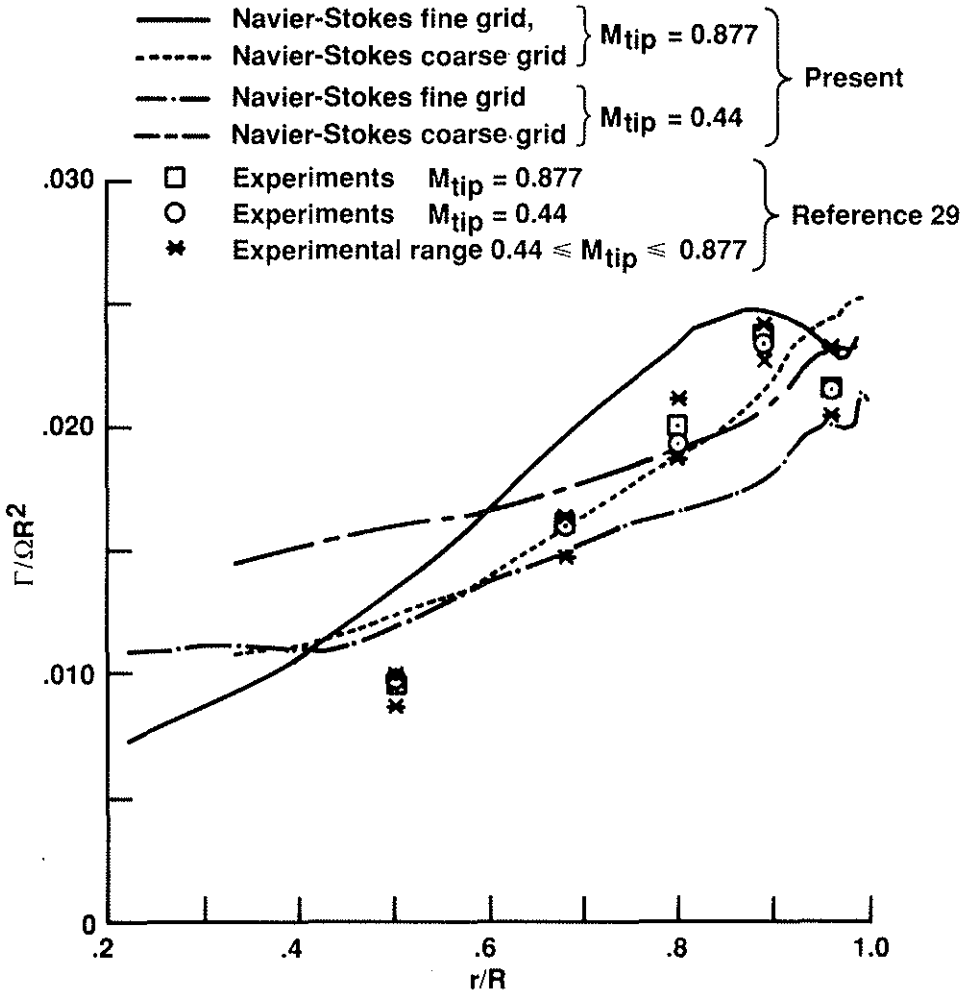

Fig. 6 Comparison of bound circulation distribution for the case of collective pitch $\theta = 8°$ with tip speeds of $M_{tip} = 0.44$ and 0.877.

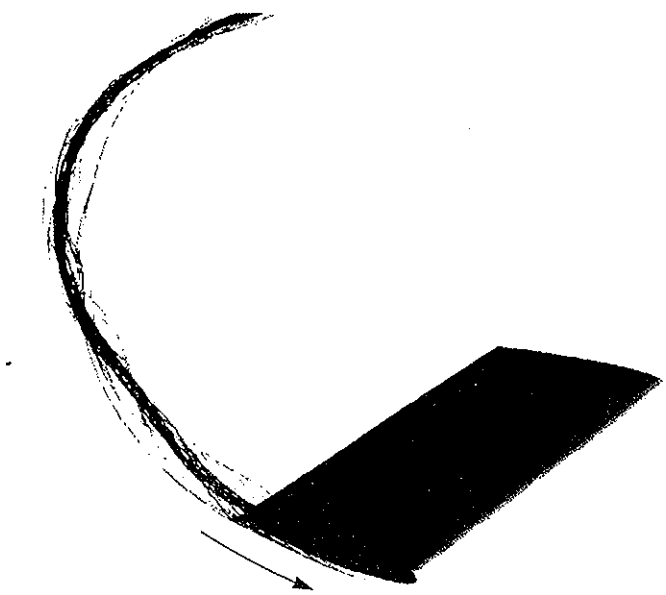

Fig. 7 Calculated tip vortex particle flow details showing the near-field view for the condition $M_{tip} = 0.794$, $\theta = 12°$, and $\mathrm{Re} = 3.55 \times 10^6$.

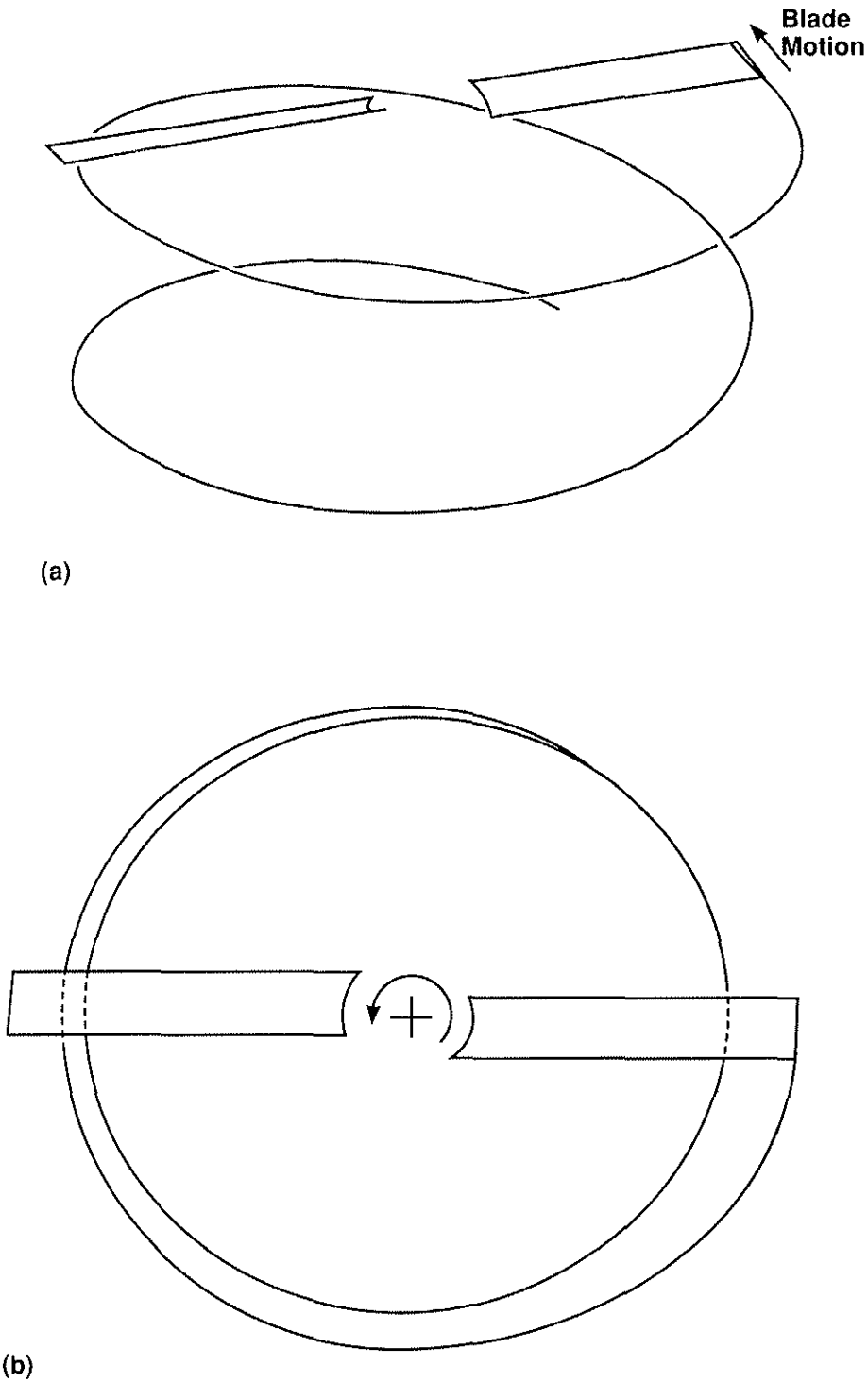

Fig. 8 Calculated tip vortex trajecotry for the flow conditions of Fig. 7; a) view showing the captured tip vortex path and its vertical descent, and b) view highlighting the contraction of the wake.

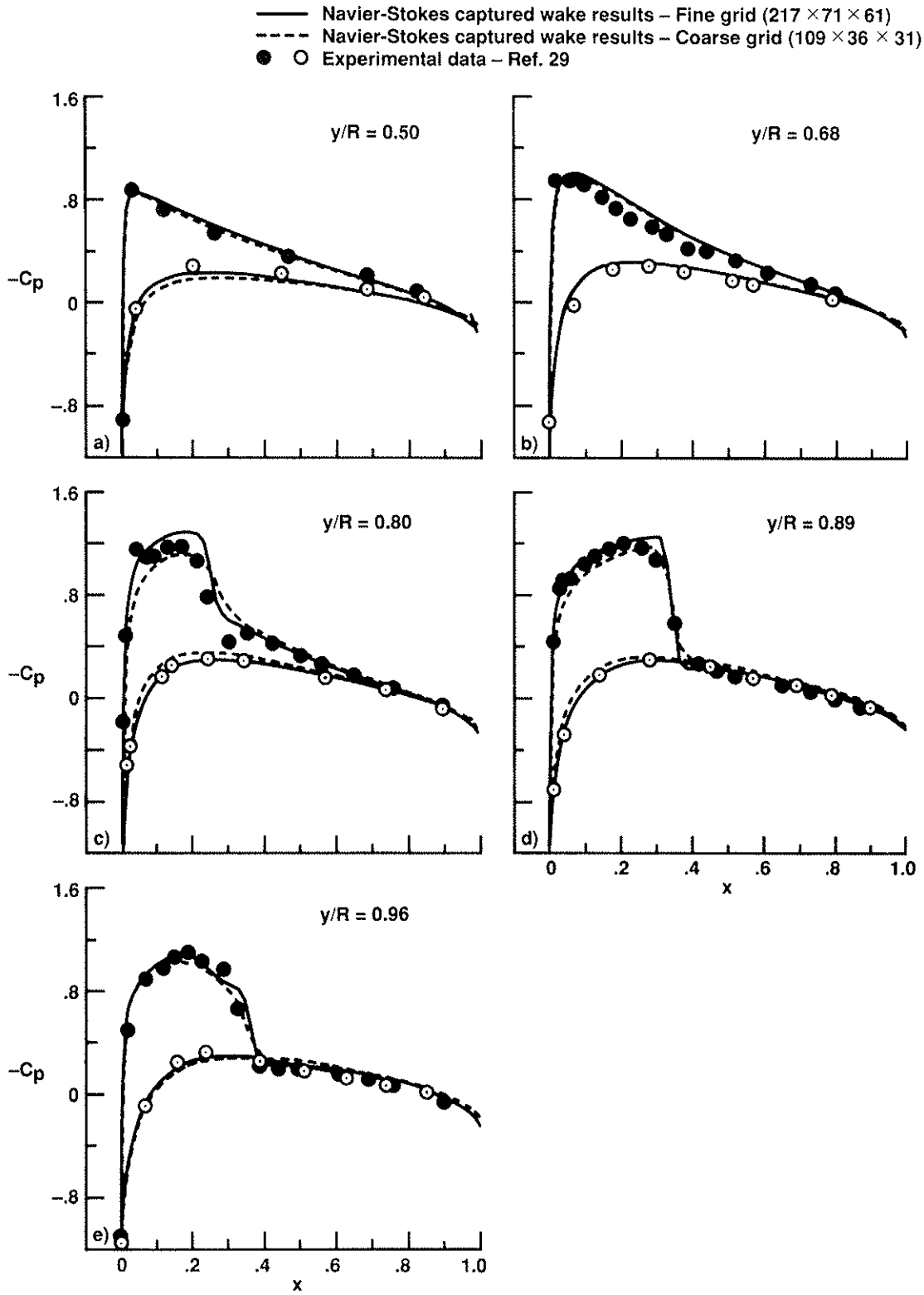

Fig. 9 Comparison of surface pressures with coarse and fine grids for the case of $M_{tip} = 0.877$, $\theta = 8°$, and $Re = 3.93 \times 10^6$.

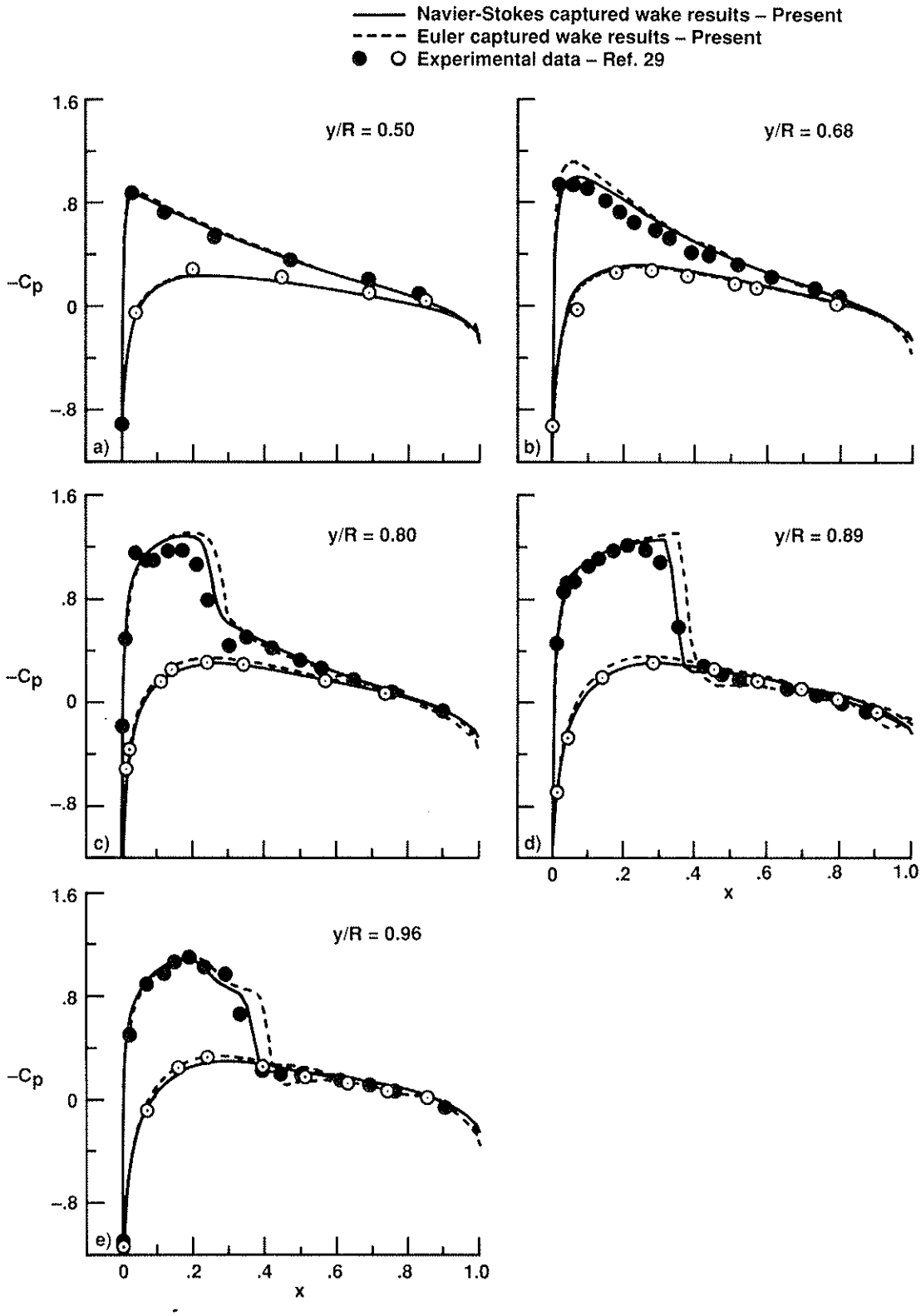

Fig. 10 Comparison of surface pressures for Euler and Navier-Stokes solutions; $M_{tip} = 0.877$, $\theta = 8°$, and $Re = 3.93 \times 10^6$.